Effects of Electrical Contact on Unstressed Patch Antenna Sensors

Liyu Xie, *Member, IEEE*, Zeyu Li, Songtao Xue, Wensheng Lu, Guochun Wan, *Member, IEEE*, and Wei Zang

***Abstract*—To avoid the bearing stress on the monolithic patch antenna sensor for material deformation sensing, the unstressed patch antenna sensor using multiple patch components has been proposed for easy deployment. A typical unstressed sensor utilizes the relative position between a shorted subpatch and a radiation patch as the deformation-sensing unit. However, the electrical contact condition between two patches and copper rusting will affect the performance and reliability of the unstressed sensor during practical application. In this article, the authors alleviate this effect by applying conductive grease between the shorted subpatch and the radiation patch. The equivalent circuit of an unstressed sensor with a shorted subpatch is established first. The different electrical contact conditions are regarded as different capacitors and resistances in this model. Both simulations and experiments are conducted to investigate the effect of different contact conditions on the sensitivity of the sensor. Furthermore, the authors conducted experiments on patch antenna sensor with a copper-coated surface that had experienced rusting. The finding reveals that applying copper-containing conductive grease between the shorted subpatch and the radiation patch enhances sensitivity and reliability of the sensor, resulting in an improvement of up to 32%.**

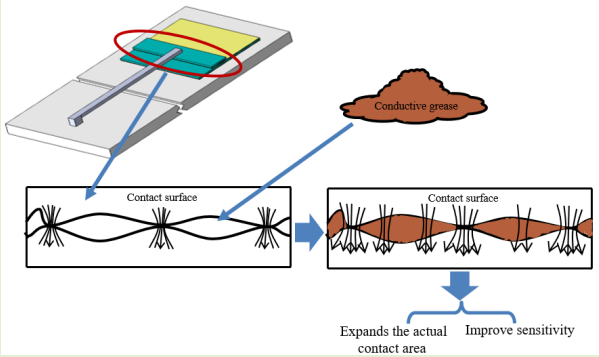

***Index Terms*— Electrical contact, rusted copper surfaces, sensing sensitivity, unstressed patch antenna.**

I. Introduction

A. Research Background

With the exponential growth of essential utilities, such as buildings, bridges, and dams worldwide, the management and maintenance of an ever-increasing number of aging facilities have become a pressing concern [1]. Under the action of long-term loads and environmental factors, various types of deformation inevitably develop within structures. Deformation frequently constitutes a pivotal factor in structural failure, adversely affecting the stability and service life of the structure, especially by diminish load-bearing capacity, durability [2], and potentially culminating in abrupt structural collapse. Consequently, deformation is a crucial factor to be employed for evaluating the health state of the equipment structure [3].

B. Prior Works

In recent years, various deformation monitoring techniques have progressively showcased their respective merits. However, it is imperative to acknowledge that each method is accompanied by inherent limitations. For example, fiber-optic-based sensors [4], [5], piezoelectric-based sensors [6], [7], [8], and deformation-sensing methods based on multi-sensor inputs and data fusion [9] usually necessitate cable power supply and data transmission for monitoring, leading to complex installation and elevated labor costs. On the other hand, monitoring techniques based on enhanced visual recognition offer the advantage of being noncontact [10], [11], [12]. Nevertheless, this method requires further refinement in terms of sensitivity for deformation detection and necessitates

Manuscript received 20 November 2023; revised 13 March 2024; accepted 13 March 2024. Date of publication 2 April 2024; date of current version 15 May 2024. This work was supported in part by the National Natural Science Foundation of China under Grant 52078375 and Grant 52178298 and in part by the Top Discipline Plan of Shanghai Universities-Class I. The associate editor coordinating the review of this article and approving it for publication was Prof. Xingwang Li. *(Corresponding author: Wei Zang.)*

Liyu Xie, Zeyu Li, and Wensheng Lu are with the Department of Disaster Mitigation for Structures, Tongji University, Shanghai 200092, China (e-mail: liyuxie@tongji.edu.cn; 2232521@tongji.edu.cn; wally@tongji.edu.cn).

Songtao Xue is with the Department of Disaster Mitigation for Structures, Tongji University, Shanghai 200092, China, and also with the Department of Architecture, Tohoku Institute of Technology, Sendai 982-8577, Japan (e-mail: Xue@tongji.edu.cn).

Guochun Wan is with the Department of Electronic Science and Technology, Tongji University, Shanghai 200092, China (e-mail: wanguochun@tongji.edu.cn).

Wei Zang is with the College of Architecture and Urban Planning, Tongji University, Shanghai 200092, China (e-mail: zang@tongji.edu.cn).

Digital Object Identifier 10.1109/JSEN.2024.3379581

that the monitored surface of the component must remain unobscured [13], [14].

Over the past few years, the realm of passive Internet of Things (IoT) has experienced rapid growth, with passive sensors assuming a pivotal role in the monitoring domain [15]. Passive sensors eliminate the need for batteries or wired power supply, relying instead on external energy sources for data transmission and reception [16], [17]. The foundation of passive IoT implementation rests upon radio frequency identification (RFID) [18], [19] or near-field communication (NFC) [20], enabling data transmission and reception through radio waves. This approach offers distinct advantages, including cost-effectiveness, uncomplicated installation, and ease of maintenance. In comparison with conventional sensors, passive sensors prove to be better suited for practical monitoring projects [21].

Antenna sensors are extensively employed as common passive wireless sensors in the domain of structural health monitoring [22]. In contrast to other conventional sensors, antennas have the dual capability to serve as both sensing and data transmission units. This unique feature empowers its capability in passive wireless structural monitoring. However, conventional monolithic patch antenna sensors typically rely on monitoring crack and displacement through the change in electromagnetic parameters of the antenna when subjected to stretching or tearing. This sensing approach is substantially influenced by shear hysteresis effects and insufficient bonding strength, thereby presenting some limitations [23]. Such as limited-service life and susceptibility to the characteristics of the bonding adhesive significantly affect its performance. Aiming at the problems affecting the accuracy of crack sensing, Bhattacharyya et al. [24] introduced an additional tag antenna positioned in the near field of a rectangular patch antenna. The separation between the patch antenna and the tag antenna varied in response to displacements, facilitating the correlation of structural deformations with changes in the backscattered signal power amplitude of the antenna. Caizzone and Di Giampaolo [25] and Caizzone et al. [26] proposed a crack sensor made of two mutual coupling planar-inverted F antennas. It represented the change in displacement between antennas by a change in the phase of the coupled antennas. However, in the existing literature, such as [27] and [28], it suggests that in NFC, the electromagnetic radiation field often needs to be modeled using near-field spherical waves. Nevertheless, spherical waves tend to exhibit nonlinear phase characteristics, which pose difficulties in accurately assessing the channel propagation characteristics of antenna sensor systems. Consequently, this affects the precise calibration of sensors. In addition, Xue et al. [23] proposed an unstressed patch antenna sensor with overlapping subpatch. This approach detects cracks or deformations within a structure by measuring the relative displacement between the two components. The relative displacement between the subpatch and the upper radiation patch results in a variation in the current flow length along the patch antenna's surface, leading to a shift in the resonant frequency of the patch antenna. Nonetheless, in practical engineering testing and application, Xue et al. [23] discovered a challenge in eliminating the air gap between the subpatch and the upper radiation patch. Achieving complete contact and a flawless shorting connection between the two components remains difficult. Li et al. [2] introduced an off-center fed patch antenna sensor featuring an overlapping subpatch suitable for engineering applications to concurrently sense temperature and strain. However, Li et al. [2] encountered challenges in addressing the issue of the contact between the subpatch and the radiation patch. To solve this problem, Li et al. [2] employed an acrylic fixture to guarantee a consistent contact area between the subpatch and the upper radiation patch. Nevertheless, utilizing a fixture for fixation adversely affects the relative displacement of the subpatch concerning the upper radiation patch. Besides, Xie et al. [29] introduced a passive unstressed wireless accelerometer sensor featuring overlapping subpatch. In this design, both the patch antenna and the overlapping subpatch utilize thicker dielectric substrates to mitigate the influence of air gaps between the contact surfaces. However, the challenge lies in the difficulty of completely alleviating the air gap between the contact surface and improving reliability.

Analyzed from the microscopic level, this issue can be attributed to the inherent roughness and irregularity of any processed surface. Such surfaces typically consist of only a limited number of protruding points or minor contact areas between the two conductors in contact [30]. This characteristic is pertinent to factory-processed antenna sensors with overlapping subpatch. Consequently, due to the limited contact areas, these sensors encounter challenges, such as diminished sensitivity and signal loss during operation.

Especially, as the service life of the patch antenna sensor extends, the copper overlay part of the patch antenna sensor may undergo chemical reactions with water vapor and atmospheric oxygen, forming a layer of oxidized film covering the patch [31], [32]. This process increases the contact resistance between the contact surfaces, leading to a decline in sensor performance. Such deteriorating conditions are not conducive to the sensor's long-term usability.

Similarly, electrical contact issues of this nature are prevalent across a wide spectrum of electrical equipment, automated control systems, and information transmission systems. The quality of electrical contact plays a pivotal role in determining the reliability and stability of both signal and power transmission [33]. Usually, to ensure the effectiveness of the contact, pressure is applied to the two conductors in contact. In power systems, the application of conductive grease stands out as an effective means to enhance the quality of electrical contact, reducing contact resistance, improving the overall quality of electrical connections, and safeguarding power equipment [34]. Conductive grease is a high-performance neutral conductive material, primarily composed of a thickened base oil with the incorporation of conductive additives, imparting oxidation, and corrosion resistance properties to create a soft paste. When applied to the conductor's contact surface, it effectively expands the actual contact area, subsequently diminishing contact resistance and augmenting transmission efficiency [35]. In addition, conductive grease can serve as an effective oil sealant on the contact surface, thereby mitigating the impact of air and corrosive gases, reducing corrosion

and oxidation, and enhancing the reliability of electrical contacts. Exploiting the operating principles of conductive grease enables the resolution of contact-related challenges in patch antenna sensors with shorted overlapping subpatch.

C. Main Contributions

In this article, based on the analysis of the equivalent circuit of patch antenna with shorted overlapping subpatch and the properties of various types of conductive grease materials, conductive grease was used to improve contact surfaces' electrical contact conditions. Both simulations and experiments are conducted to investigate the effect of different contact conditions on the sensitivity of the sensor. The main contributions are summarized as follows.

1) The objective contact conditions of the unstressed patch antenna sensors are taken into account. Equivalent circuits of the sensors and their resonance frequency approximation formulas are derived under practical circumstance.
2) The effect of different contact conditions on the sensitivity of unstressed patch antenna sensors is investigated by simulation and experimental analysis.
3) Conductive grease was applied to patch antenna sensors exhibiting oxidative rust, and a comparison was conducted before and after the treatment.

The rest of this article is organized as follows. Section II presents the equivalent numerical analysis of contact effects. In Section III, we simulated the contact conditions with Ansoft high-frequency structure simulator (HFSS). Materials were parametrically modeled and investigated the influence of different contact conditions on sensor sensitivity. In Section IV, we provide the experiment results and discussions, and our conclusions are drawn in Section V.

II. Equivalent Numerical Analysis of Contact Effects

A. Mechanism of Contact Surface

Fig. 1 depicts the patch antenna with overlapping subpatch sensor, suitable for crack monitoring. As the crack expands, the upper radiation patch undergoes relative displacement with respect to the overlapping subpatch. This motion induces a modification in the electrical path length of the current flow within the patch antenna sensor, subsequently changing the antenna's resonant frequency. In the ideal scenario, the contact surface between the subpatch and upper radiation patch exhibits complete contact, resulting in a perfect electrical contact. However, in real-world situations, as shown in Fig. 2, only a limited number of protruding points or small contact areas exist between the two surfaces.

These localized contact points are frequently termed "conductive spots." In actuality, the effective contact area between the conductors, when they come into contact with each other, is relatively small compared with the macroscopic contact surface, as depicted in Fig. 2. Consequently, the resistance across the contact surfaces significantly escalates as current passes through them, thereby leading to a reduction in the sensor's sensitivity, operational range, and other characteristics. This,

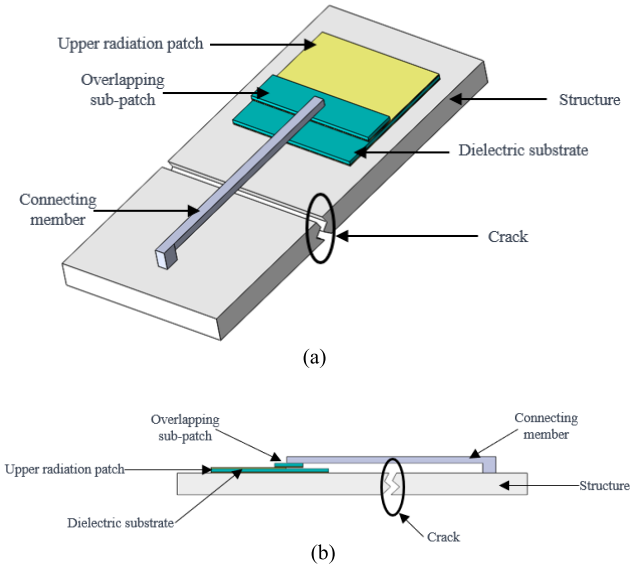

Fig. 1. Patch antenna with overlapping subpatch crack sensor. (a) Panoramic view. (b) Side view.

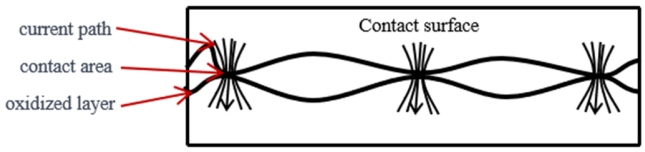

Fig. 2. Conductors contact surface under microscopic level.

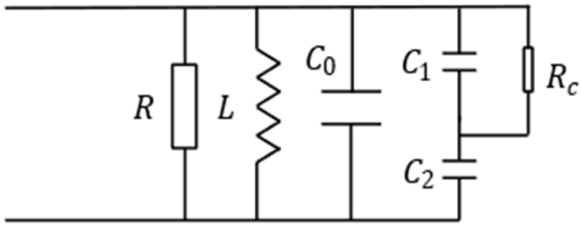

Fig. 3. Patch antenna sensor equivalent circuit.

in turn, diminishes the sensor's sensitivity to detect minor structural deformations within the building. Considering the aforementioned electrical contact characteristics, the contact surfaces are treated as a parallel combination of capacitance and resistance and are further analyzed in Section II-B.

B. Equivalent Circuit of Unstressed Patch Antenna Sensor in Practical Condition

An equivalent circuit analysis of this patch antenna sensor in a practical condition is depicted in Fig. 3. In this analysis, the air gap between the overlapping components is represented as an equivalent capacitance C_1, while the contact points between the conductors within the gap are denoted as an equivalent contact resistance R_C.

By analyzing the equivalent circuit, where the resistance and inductance of the nonoverlapping section are denoted as R and L, respectively, the nonoverlapping part can be considered as an equivalent capacitance C_0, and the overlapping part is treated as an equivalent capacitance C_2. The individual

distributed capacitances can be expressed using the equations as follows:

$$C_0 = \frac{W(L_1 - L_0)\varepsilon}{h_1} \tag{1}$$

$$C_1 = \frac{WL_0\varepsilon_0}{h_2} \tag{2}$$

$$C_2 = \frac{WL_0\varepsilon}{h_1}. \tag{3}$$

Also, the total equivalent capacitance C_b can be expressed as follows:

$$C_b = C_0 + \frac{C_1C_2}{C_1 + C_2} = \frac{W(L_1 - L_0)\varepsilon}{h_1} + \frac{\frac{WL_0\varepsilon}{h_1} \cdot \frac{WL_0\varepsilon_0}{h_2}}{\frac{WL_0\varepsilon}{h_1} + \frac{WL_0\varepsilon_0}{h_2}} \tag{4}$$

where W represents the width of the patch antenna, L_1 denotes the length of the upper radiation patch, L_0 signifies the length of the overlapping section between the upper radiation patch and the subpatch, h_1 stands for the thickness of the radiation patch substrate, and h_0 represents the thickness of the air gap existing between the radiating patch and the subpatch.

In addition, considering the real-world scenario, it is assumed that the dielectric constants of the individual substrates are equal and are represented as ε, while the dielectric constant of the air is represented as ε_0.

For the above LC equivalent circuit, its resonant frequency can be expressed as follows:

$$f = \frac{1}{2\pi\sqrt{LC}}. \tag{5}$$

Due to the introduction of capacitive impedance, it can be assumed that the inductance of the patch antenna remains constant and is expressed by (5)

$$L = \frac{\mu h_1 L_1}{W} \tag{6}$$

where μ is the magnetic permeability of the patch.

Also, the resonant frequency approximation, after accounting for practical conditions, is presented in the following equation:

$$\begin{aligned} f &= \frac{1}{2\pi\sqrt{\frac{\mu h_1 L_1}{W}}\sqrt{\frac{W(L_1 - L_0)\varepsilon}{h_1} + \frac{WL_0\varepsilon\varepsilon_0}{\varepsilon h_2 + \varepsilon_0 h_1}}} \\ &= \frac{1}{2\pi\sqrt{\mu h_1 L_1 \varepsilon}\sqrt{\left(\left(\frac{L_1}{h_1}\right) + \left(\frac{\varepsilon_0}{\varepsilon h_2 + \varepsilon_0 h_1} - \frac{1}{h_1}\right)L_0\right)}}. \end{aligned} \tag{7}$$

Approximating (7) yields the following equation:

$$\begin{aligned} f &= \frac{\sqrt{\left(\left(\frac{L_1}{h_1}\right) - \left(\frac{\varepsilon_0}{\varepsilon h_2 + \varepsilon_0 h_1} - \frac{1}{h_1}\right)L_0\right.}}{2\pi\sqrt{\mu h_1 L_1 \varepsilon}\sqrt{\left(\left(\frac{L_1}{h_1}\right)^2 - \left(\frac{\varepsilon_0}{\varepsilon h_2 + \varepsilon_0 h_1} - \frac{1}{h_1}\right)^2 L_0^2\right)}} \\ &\approx \frac{\sqrt{\left(\frac{L_1}{h_1} - kL_0\right)}}{2\pi\sqrt{\mu h_1 L_1 \varepsilon}\frac{L_1}{h_1}} \end{aligned} \tag{8}$$

TABLE I
CRITICAL DIMENSIONS OF THE PATCH ANTENNA SENSOR

Parameters	$L_r(mm)$	$W(mm)$	$L_1(mm)$	$h_1(mm)$	$L_s(mm)$
Value	70	60	41	0.508	13

Where L_s is the length of overlapping sub-patch.

where k is a constant and determined by the following equation:

$$k = \left(\frac{\varepsilon_0}{\varepsilon h_2 + \varepsilon_0 h_1} - \frac{1}{h_1}\right). \tag{9}$$

According to (8), the resonant frequency of the patch antenna will decrease with the increasing of the overlapping section. This relationship can be utilized for sensor applications.

For this patch antenna sensor, the chosen substrate material is Rogers RT/duroid 5880, characterized by a dielectric constant $\varepsilon = 2.2$ and a thickness $h_1 = 0.508$ mm. The dielectric constant ε_0 of the air gap between the upper radiation patch and the overlapping subpatch is 1, with a thickness $h_2 = 1/10h_1$, resulting in a calculated value $k = -0.3549$ according to (9).

For typical conductive grease, its primary constituents are polyalphaolefin (PAO) [36]. Disregarding the conductive additives added to the conductive grease, a dielectric constant of $\varepsilon_1 = 2.11$ and a thickness of $h_2 = h_1$ are assumed, resulting in a calculated value of $k = -1.0048$ according to (9).

Based on the calculation results, the application of conductive grease to the contact surface between the upper radiation patch and the subpatch results in a 1.68-fold increase in the resonant frequency shift of the patch antenna. This substantial increase in resonant frequency alteration aims to enhance sensitivity, thereby augmenting the sensor's ability to detect cracks.

To confirm the effect of different contact conditions on the sensor, HFSS is employed for simulation and validation.

III. SIMULATION IN HFSS

The resonance frequency of the patch antenna sensor under study in this article is approximately 2.2 GHz, with the antenna dimensions estimated based on the calculation (10) for patch antenna resonance frequency

$$f_{mn} = \frac{c}{2\sqrt{\varepsilon}}\sqrt{\left(\frac{m}{L_r}\right)^2 + \left(\frac{n}{W}\right)^2} \tag{10}$$

where c is the speed of light, L_r is the length of the upper radiation patch, W is the width of the patch antenna, ε is the relative permittivity of the patch antenna substrate, and m and n are the resonance orders in the two directions of the length and width, respectively. The parameters of the patch antenna sensor are ascertained as detailed in Table I.

A. Simulation of Unstressed Patch Antenna Sensor Without Treatment

Fig. 4 shows the uncoated conductive grease finite-element model constructed in HFSS, utilizing the parameters specified

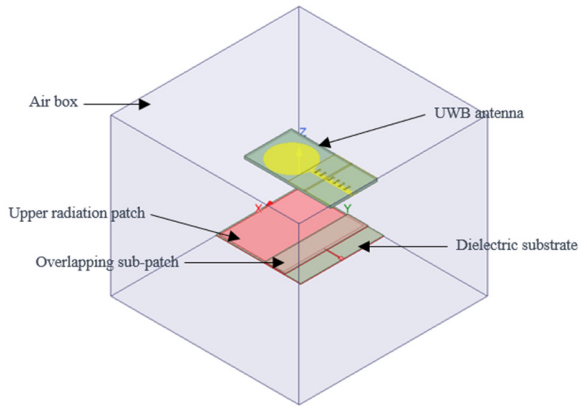

Fig. 4. Unstressed patch antenna sensor modeled in HFSS.

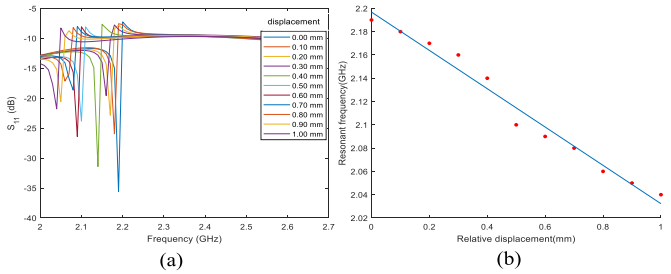

Fig. 5. (a) S_{11} curve and (b) fitting of resonant frequency and relative displacement.

in Table I. This model is composed of both overlapping subpatch and the patch antenna. The dielectric plate is composed of Rogers RT/duroid 5880, while both the overlapping subpatch and the upper radiation patch are represented as perfect E due to the minimum skin depth of electromagnetic waves in the 2.2-GHz band. The patch antenna crack sensor is arranged inside a perfectly matched layer (PML) air box with a radius of about a quarter wavelength to ensure computational accuracy of the far-field radiation. To simulate the practical interrogation of the patch antenna sensor, an ultrawideband (UWB) antenna is employed in the simulation. The unstressed patch antenna sensor is interrogated from a distance of 4 cm using the UWB emitting antenna, which generates electromagnetic waves through lumped port excitation.

To ensure the monitoring capability of the unstressed patch antenna sensor in both lengthwise directions, an initial overlap length is set between the overlapping subpatch and the upper radiation patch. Simulation is carried out incrementally in 0.1-mm steps as the subpatch gradually moves. The overlap length expands until it reaches 1 mm, signifying that the structure's cracks have been maximally extended. The simulation outcomes are illustrated in Fig. 5(a).

In Fig. 5(b), a linear relationship between the relative displacement and the resonant frequency is evident, with a linear fit coefficient of 0.9774. This coefficient suggests that the resonant frequency exhibits nearly linear variations corresponding to the displacement of the overlapping subpatch. The slope of this fit is measured at 164.5 MHz/mm, representing the sensitivity of this patch antenna sensor to sense crack.

TABLE II
ELECTROMAGNETIC MATERIAL PARAMETERS OF PAO

Parameter	Relative Permittivity	Bulk Conductivity (S/m)
Value	2.11	2.2

TABLE III
ELECTROMAGNETIC MATERIAL PARAMETERS OF SILICON OIL

Parameter	Relative Permittivity	Bulk Conductivity (S/m)
Value	11.9	0

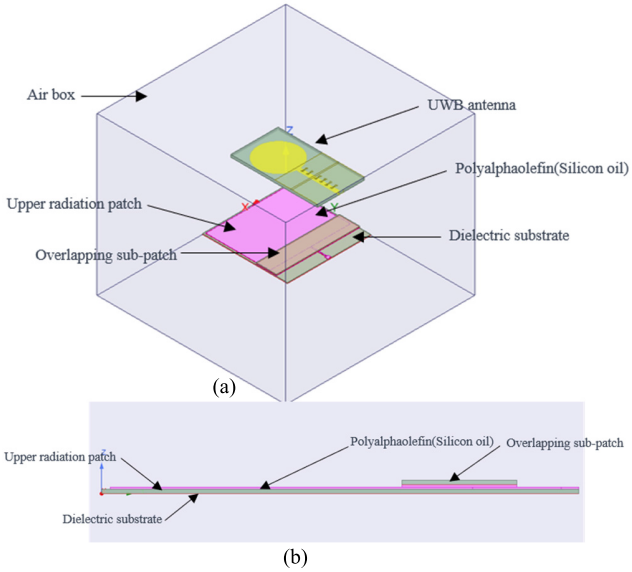

Fig. 6. Patch antenna modeled with PAO or silicon oil in HFSS. (a) Panoramic view. (b) Side view.

To simulate the unstressed patch antenna sensor treated with the application of conductive grease, two commonly used types of conductive grease are parametrically modeled in HFSS. It is worth noting that the conductive additives added within the conductive grease are minute, requiring a finer mesh division and increasing unnecessary computational load. Hence, the small conductive additives are disregarded, and the primary components of the two types of conductive grease, namely, PAO and silicon oil, are, respectively, modeled. The electromagnetic material parameters of PAO are extracted from the literature in the electrical power field [36], as detailed in Table II. For silicon oil, material parameters are sourced from the HFSS material library, with specific details provided in Table III.

B. Simulation of Unstressed Patch Antenna Sensor With Primary Components of Conductive Grease

Similar to the previous analog simulation procedure, a layer of PAO and silicone oil of the same thickness as the substrate was added between the overlapping subpatch and the upper radiating patch, respectively, as shown in Fig. 6.

The simulations were conducted under consistent conditions, and the respective results are presented in Figs. 7 and 8.

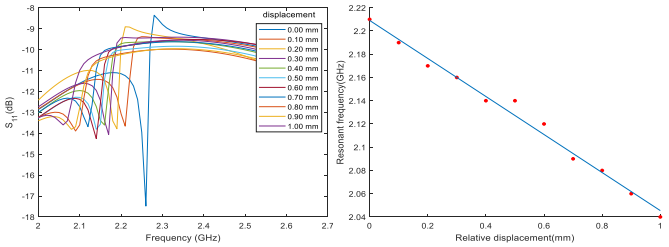

Fig. 7. Simulation results after adding PAO. (a) S_{11} curve and (b) fitting of resonant frequency and relative displacement.

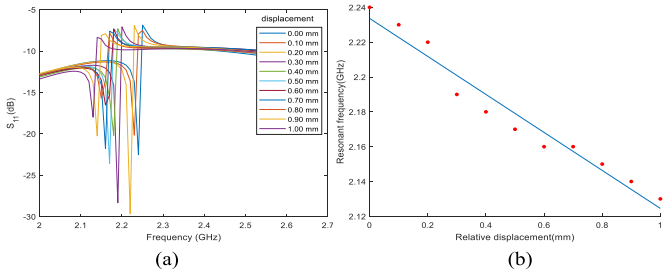

Fig. 8. Simulation results after adding silicone oil. (a) S_{11} curve and (b) fitting of resonant frequency and relative displacement.

In the results, a linear regression was performed to relate the resonant frequency to the relative displacement. The fit results are depicted in Figs. 7(b) and 8(b). For the simulation results with the addition of PAO, the linear fit coefficient is calculated to be 0.9878, suggesting an almost linear relationship between these variables. The slope of the fit is measured at 176.4 MHz/mm, representing the sensitivity of this patch antenna sensor with a PAO layer to sense crack.

Similarly, for the simulation results with the addition of silicon oil, the linear fit coefficient is calculated as 0.9594, signifying a relatively poor linear relationship. The slope of the fit measures 109.1 MHz/mm, representing the sensitivity of this patch antenna sensor with a silicon oil layer to sense crack.

C. Comparison of Simulation Results for Different Treatments

Table IV demonstrates the comparison of the results for three different simulation cases. The sensors' sensitivity is notably improved through the incorporation of materials that serve as the principal components of the conductive grease, with copper and graphite as the conductive additives. However, it is important to note that the enhancement is not entirely precise, as the conductive grease is not simulated comprehensively with all the materials. Further verification through experiments is required, and the experimental details will be expounded upon in next section. Notably, the conductive additive in the conductive grease with silicone oil as the primary component is silver powder. However, an intriguing observation was made as the sensor's sensitivity decreased after the addition of silicone oil. This phenomenon can be attributed to the following reason.

In the preceding section on performance improvement analysis, it was evident that when the primary component of the applied conductive grease is PAO, a noticeable sensitivity enhancement effect is achieved. Now, with its primary component replaced by silicone oil, and disregarding the added conductive material, the conductive grease exhibits a dielectric constant of $\varepsilon_1 = 11.9$ and a thickness of $h_2 = h_1$, resulting in a calculated value of $k = -0.3071$. In comparison with the untreated results, the use of conductive grease with silicone oil as the primary component does not yield a significant improvement in sensor sensitivity. However, it is worth noting that this specific conductive grease contains added silver as the conductive material, which, in comparison with other conductive materials, such as copper, offers lower resistivity and reduced energy loss at the contact surface. In practice, the potential enhancement effect necessitates further verification through experiments.

TABLE IV
COMPARISON OF SIMULATION RESULTS FOR DIFFERENT TREATMENTS

Treatment	Untreated	Polyalphaolefin	Silicon oil
Linear Fit Coefficient	0.9774	0.9878	0.9594
Sensitivity (MHz/mm)	164.5	176.4	109.1
Sensitivity Comparison	—	+7.2%	-33.7%

IV. EXPERIMENTS AND RESULTS

This section is divided into two parts. The first part validates the improved performance of unstressed patch antenna sensors after changing the contact conditions by applying conductive grease. It also compares the effects of different conductive greases used in experiments. The next part experimentally validates the performance enhancement of unstressed patch antenna sensors with oxidative rust after changing the contact conditions by the application of conductive grease. This separation is necessitated by the constraints posed by simulation software in modeling durability, leading to the need for experimental verification.

A. Validation of Varying Sensitivity of Unstressed Patch Antennas With Different Contact Conditions

Building upon the prior theoretical analysis and simulation, this section aims to validate the sensitivity enhancement of unstressed patch antenna with different contact conditions through a series of experiments. The experimental setup is designed, as illustrated in Fig. 9.

The experimental setup comprises a crack simulator, a patch antenna sensor, and an interrogation section, as shown in Fig. 9(a)–(c). The crack simulator consists of a base plate, a foam fixed table, and a movable table. The movable table can be adjusted in 0.01-mm steps relative to the fixed table, simulating crack extension using a side spiral micrometer bar. Foam was selected for the fixed table to minimize electromagnetic interference caused by the crack simulator. Both tables were securely glued to a rigid acrylic base plate to reduce unintended motion of the experimental setup prior to conducting the experiments. Subsequently, the patch antenna sensor was glued to the fixed table of the crack simulator, while the subpatch was connected to the movable table using an acrylic connecting rod. This configuration allowed for the

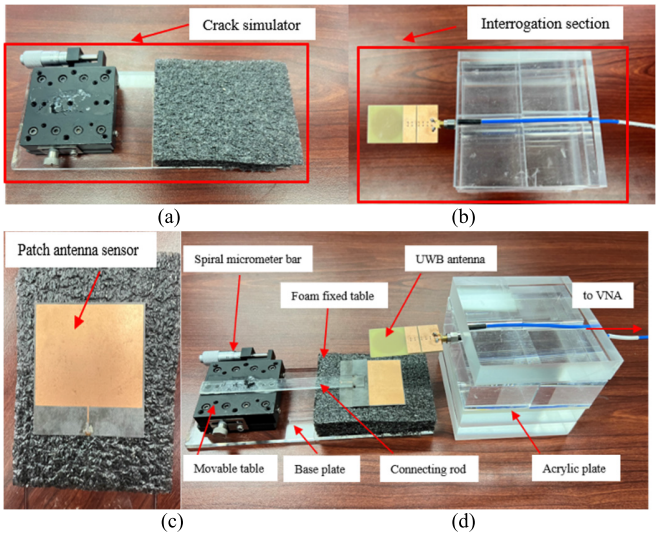

Fig. 9. Experimental setup. (a) Crack simulator. (b) Interrogation section. (c) Patch antenna sensor. (d) Overall experimental setup.

TABLE V
PARAMETERS OF CONDUCTIVE GREASE

Products	FUTU 572	JUNE SD-001	ITW CW7100
Primary Component	Polyalphaolefin	Polyalphaolefin	Silicon oil
Conductive Additive	Copper powder	Graphite powder	Silver powder

adjustment of the spiral micrometer bar to simulate real-world crack occurrence and extension by achieving relative displacement between the two tables.

The patch antenna sensors employed in the experiments were precision-machined and fabricated strictly to the simulation dimensions. The dielectric substrate material selected was Rogers RT/duroid 5880, which was coated with standard electrolytic copper. A UWB antenna was utilized to transmit plane waves to the designed patch antenna sensor and receive backscattering signals. To maintain consistency with the simulation, the UWB antenna was positioned directly above the sensor at a distance of 4 cm, separated by a 4-cm-thick acrylic plate.

A vector network analyzer (VNA) is linked to the UWB antenna through a coaxial cable to collect and analyze signals reflected from the patch antenna crack sensor. The VNA sweep range is 2–3 GHz, facilitating a more comprehensive observation of resonant frequency generated by the patch antenna crack sensor. Throughout the experiment, the subpatch is incrementally adjusted in 0.1-mm increments to simulate crack expansion. The local curve of the sensor's return loss at each step is captured, as illustrated in Fig. 10(a).

The resonant frequency at the local minimum of each curve was extracted to obtain a linear fit of the resonant frequency to the crack width, as shown in Fig. 10(b). In the diagram, the linear fit coefficient is calculated to be 0.9916, suggesting linear relationship between these variables. The slope of the fit is measured at 173.0 MHz/mm, representing the sensitivity of this patch antenna sensor to sense crack.

The overlapping subpatch was removed from the setup and coated with conductive grease. The conductive greases used in

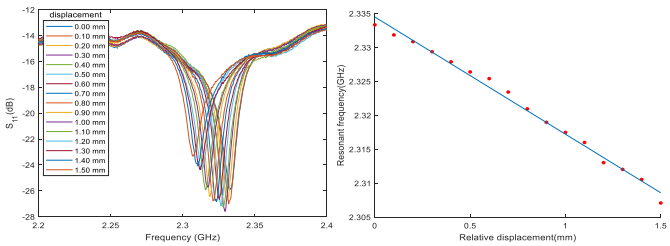

Fig. 10. (a) S_{11} curve and (b) fitting of resonant frequency and crack width.

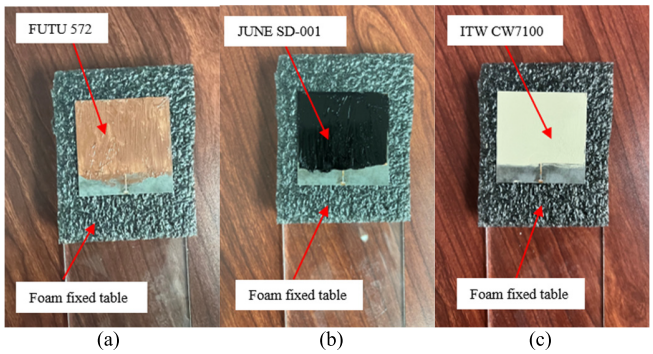

Fig. 11. Patch antenna sensor after coated with conductive grease. (a) FUTU 572. (b) JUNE SD-001. (c) ITW CW7100.

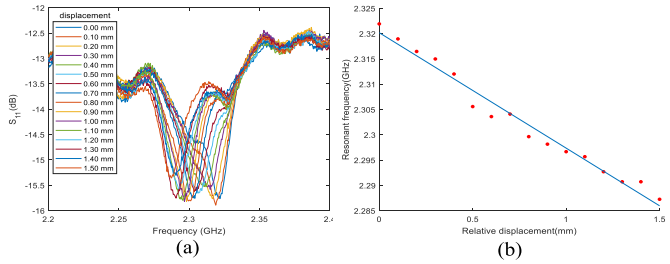

Fig. 12. Results after treatment with FUTU 572. (a) S_{11} curve and (b) fitting of resonant frequency and crack width.

the experiment included FUTU 572 copper conductive paste, Japan JUNE SD-001 graphite conductive grease, and the U.S. ITW CW7100 silver conductive grease. Specific parameters can be found in Table V.

In accordance with the specifications for applying conductive grease, the upper radiation patch on the sensor is subject to a straightforward cleaning process. A uniform application of conductive grease is achieved on the upper radiation patch using a plastic scraper, as shown in the Fig. 11. Subsequently, the experimental setup is assembled and tested following the previously outlined requirements.

Similarly, the subpatch was incrementally adjusted in 0.1-mm steps throughout the experiment. Local return loss curves were obtained for each step, showcasing the transducers treated with FUTU 572 copper conductive paste and JUNE SD-001, as depicted in Figs. 12(a) and 13(a).

The resonant frequencies at the local minimum of each curve in the two sets of results were independently extracted, and linear fit plots of resonant frequency with crack width were generated, as illustrated in Figs. 12(b) and 13(b).

TABLE VI
COMPARISON OF EXPERIMENTS RESULTS FOR DIFFERENT TREATMENTS

Treatment	Untreated (experiment)	FUTU 572	JUNE SD-001	ITW CW7100
Linear Fit Coefficient	0.9916	0.9791	0.9804	0.9726
Sensitivity (MHz/mm)	173.0	228.5	161.0	14.2
Sensitivity Comparison	—	+32.1%	-6.9%	-91.8%

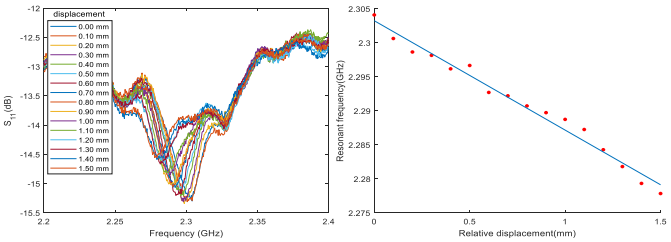

Fig. 13. Results after treatment with JUNE SD-001. (a) S_{11} curve and (b) fitting of resonant frequency and crack width.

As shown in Fig. 14, the patch antenna sensor treated with ITW CW7100 exhibits limited effectiveness within the 0–1-mm range. Consequently, further investigation was carried out with a 0.5-mm crack extension step, and the results are presented in Fig. 15(a).

The resonant frequency at the local minimum of each curve was extracted to obtain a linear fit of the resonant frequency to the crack width, as shown in Fig. 15(b).

Table VI illustrates the comparison of sensitivity and linear fitting coefficients for the sensors following various contact conditions. These results are compared with the simulation results, leading to the following conclusions.

1) The sensitivity of the untreated patch antenna sensor exhibits no substantial difference between the experimental and simulated results, indicating the well design of the crack sensor.
2) Similar to the simulation, the sensitivity of the patch antenna sensor to crack width can be enhanced by introducing a conductive grease with PAO as the primary component. In comparison with the simulation, the experimental crack sensors, when treated with conductive grease, exhibit a notably enhanced sensitivity. This improvement is attributed to the facilitating effect of conductive additives in the conductive grease on current flow.
3) According to Fig. 16, the sensitivity of the sensors treated with JUNE SD-001 and ITW CW7100 conductive grease did not exhibit improvements in the experiments. In particular, the latter exhibited a significant reduction in sensitivity during the experiments. The reason behind this observation is the suboptimal friction performance of these two types of conductive grease. They introduce a viscous effect, which impedes the smooth movement of the movable table. As a result, the subpatch and the upper radiation patch experience incorrect movement, leading to poor performance.

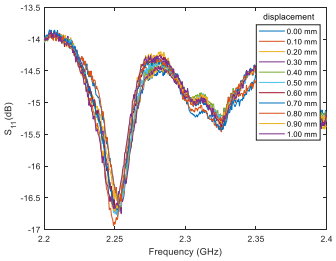

Fig. 14. Results after treatment with ITW CW7100.

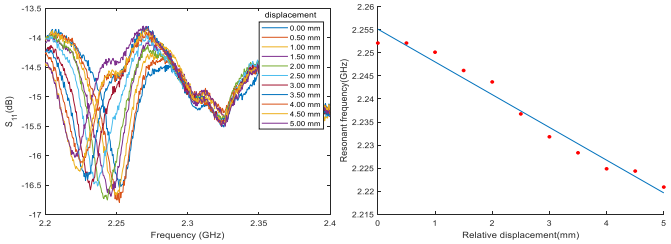

Fig. 15. Results after treatment with ITW CW7100. (a) S_{11} curve and (b) fitting of resonant frequency and crack width.

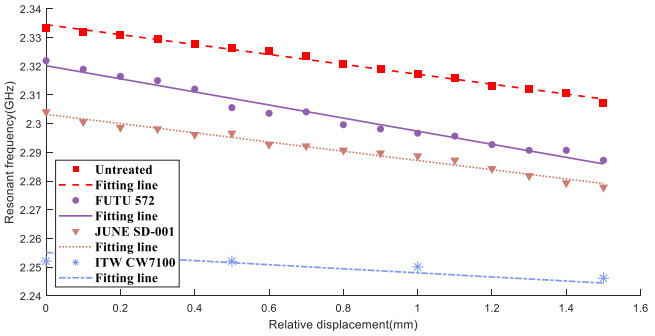

Fig. 16. Comparison of fitting lines under different electrical contact conditions.

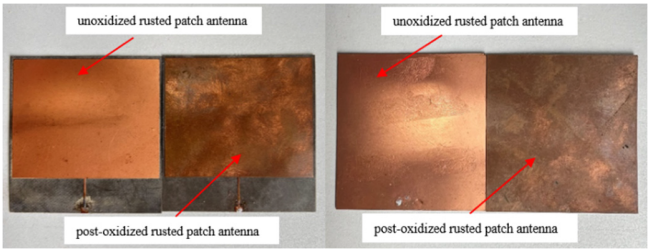

Fig. 17. Normal antenna and oxidized antenna. (a) Front view. (b) Back view.

B. Validation of Sensitivity Enhancement for Unstressed Patch Antenna Sensors With Oxidative Rust

In this experiment, an unstressed patch antenna sensor of the same dimensions as previously mentioned was utilized. The sensor had been stored in a laboratory environment for 14 months, and an oxide film formed on the sensor surface is depicted in Fig. 17.

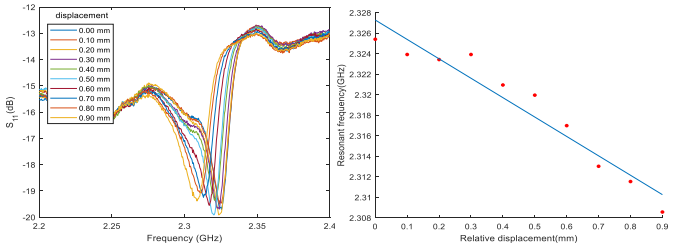

Fig. 18. Results of postoxidized rusted patch antenna sensor. (a) S_{11} curve and (b) fitting of resonant frequency and crack width.

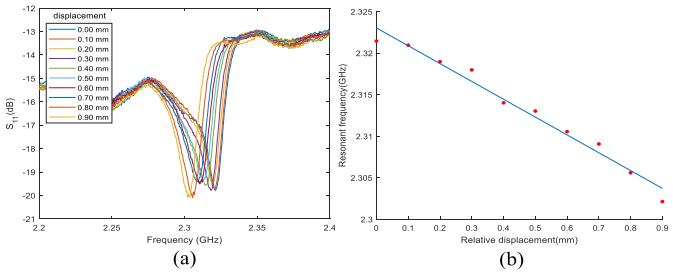

Fig. 19. Results of postoxidized rusted patch antenna sensor after treatment with FUTU 572. (a) S_{11} curve and (b) fitting of resonant frequency and crack width.

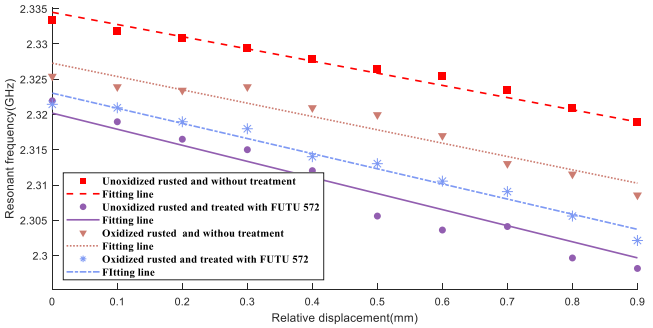

Fig. 20. Comparison of fitting lines under different electrical contact conditions.

TABLE VII
COMPARISON OF EXPERIMENTS RESULTS BEFORE AND AFTER TREATMENTS

Series	Unoxidized rusted sensor (untreated)	Unoxidized rusted sensor (treated*)	Oxidized rusted sensor (untreated)	Oxidized rusted sensor (treated*)
Linear Fit Coefficient	0.9916	0.9791	0.9292	0.9767
Sensitivity (MHz/mm)	173.0	228.5	95.0	164.1
Sensitivity Comparison	—	+32.1%	—	+72.7%

* Treated means treated with FUTU 572.

The experiment followed the same procedures and conditions as described in Section IV-A. The crack was incrementally expanded in 0.1-mm steps, reaching a maximum of 0.9-mm expansion. Local curves of the return loss for the untreated oxidized patch antenna sensor were obtained, as illustrated in Fig. 18(a).

The resonant frequency at the local minimum of each curve was extracted to obtain a linear fit of the resonant frequency to the crack width, as shown in Fig. 18(b). The linear fit coefficient is calculated to be 0.9292, suggesting a relatively poor linear relationship between these variables. The slope of the fit measures 95.0 MHz/mm, representing the sensitivity of this postoxidized rusted patch antenna sensor to sense crack.

Then, the overlapping subpatch of postoxidized rusted patch antenna was removed from the experimental setup and coated with conductive grease. Subsequently, a coating process was carried out using FUTU 572 copper conductive paste. The experiment was then repeated with the same procedures to obtain the local return loss curves of the patch antenna sensor after applying conductive grease, as depicted in Fig. 19(a).

Similarly, the resonant frequency at the local minimum of each curve was extracted to obtain a linear fit of the resonant frequency to the crack width, as shown in Fig. 19(b). The linear fit coefficient is calculated to be 0.9767, suggesting an almost linear relationship between these variables. The slope of the fit measures 164.1 MHz/mm, representing the sensitivity of this postoxidized rusted patch antenna sensor to sense crack after treatment with FUTU 572.

Table VII presents a comparison of the experimental results for the unoxidized rusted patch antenna sensors before and after applying the conductive grease, as well as the postoxidized rusted patch antenna before and after applying FUTU 572. The analysis of these results leads to the following conclusions.

1) The oxidative rust of patch antenna sensors can impact their sensitivity and linearity, particularly when they are stored improperly. This underscores the importance of addressing issues related to the presence of oxide films between contact surfaces and enhancing oxidation resistance to maintain optimal sensor performance.
2) According to Fig. 20, applying conductive grease to the patch antenna sensor after oxidation and rust enhances the sensor's sensitivity. This improvement is due to the conductive additives in the grease, which enables an efficient current path between the shorted contact surfaces, ultimately improving the sensor's performance.

V. CONCLUSION

In this article, the performance of patch antenna sensors with overlapping subpatch is compared under different contact conditions. By applying conductive grease to the contact surface, the sensitivity of these sensors to detect small cracks can be significantly improved, with an enhancement of up to 32%. Furthermore, the influence of natural oxidative rust on patch antenna sensors is discussed. It is confirmed that the application of conductive grease on the contact surface enhances both linearity and sensitivity of the sensors after oxidative rust. This improvement contributes to extending the service life of these sensors in engineering applications.

Despite the promising results presented in this article, several ongoing challenges require attention. These encompass selecting the primary components of the conductive grease and assessing the influence of temperature and humidity on this treatment method. Besides, it is crucial to protect patch antenna sensor surfaces from rust after applying conductive grease and to find ways to minimize rust effects. In future applied research, one solution to reduce the rust effect of these sensors is to use tightly sealed packaging. Thus, the

sensors can maintain reliable electrical contact. Addressing these challenges is essential for facilitating the widespread application of these sensors in the future.

REFERENCES

[1] J. M. W. Brownjohn, "Structural health monitoring of civil infrastructure," *Philos. Trans. Roy. Soc. A, Math., Phys. Eng. Sci.*, vol. 365, no. 1851, pp. 589–622, Feb. 2007, doi: 10.1098/rsta.2006.1925.

[2] X. Li, S. Xue, L. Xie, G. Wan, and C. Wan, "An off-center fed patch antenna with overlapping sub-patch for simultaneous crack and temperature sensing," *Smart Mater. Struct.*, vol. 31, no. 9, 2022, Art. no. 095036, doi: 10.1088/1361-665X/ac80e0.

[3] T. Li, D. Wu, M. O. Khyam, J. Guo, Y. Tan, and Z. Zhou, "Recent advances and tendencies regarding fiber optic sensors for deformation measurement: A review," *IEEE Sensors J.*, vol. 22, no. 4, pp. 2962–2973, Feb. 2022, doi: 10.1109/JSEN.2021.3138091.

[4] X. Gu, Z. Chen, and F. Ansari, "Embedded fiber optic crack sensor for reinforced concrete structures," *Struct. J.*, vol. 97, no. 3, pp. 468–476, 2000.

[5] T. Han, G. Wu, and Y. Lu, "Crack monitoring using short-gauged Brillouin fiber optic sensor," *Measurement*, vol. 179, Jul. 2021, Art. no. 109461, doi: 10.1016/j.measurement.2021.109461.

[6] A. Kocherla, M. Duddi, and K. V. L. Subramaniam, "Embedded PZT sensors for monitoring formation and crack opening in concrete structures," *Measurement*, vol. 182, Sep. 2021, Art. no. 109698, doi: 10.1016/j.measurement.2021.109698.

[7] P. S. Sumant and S. K. Maiti, "Crack detection in a beam using PZT sensors," *Smart Mater. Struct.*, vol. 15, no. 3, pp. 695–703, 2006, doi: 10.1088/0964-1726/15/3/004.

[8] T. Wang, B. Tan, M. Lu, Z. Zhang, and G. Lu, "Piezoelectric electromechanical impedance (EMI) based structural crack monitoring," *Appl. Sci.*, vol. 10, no. 13, p. 4648, 2020, doi: 10.3390/app10134648.

[9] P. Li, Y. Qi, C. Yuan, Q. Kong, and B. Xiong, "A deep learning-based vision enhancement method for UAV assisted visual inspection of concrete cracks," *Smart Struct. Syst.*, vol. 27, no. 6, pp. 1031–1040, 2021, doi: 10.12989/sss.2021.27.6.1031.

[10] Q. Gong, L. Zhu, Y. Wang, and Z. Yu, "Automatic subway tunnel crack detection system based on line scan camera," *Struct. Control Health Monit.*, vol. 28, no. 8, p. e2776, 2021, doi: 10.1002/stc.2776.

[11] S. Y. Kong, J. S. Fan, Y. F. Liu, X. C. Wei, and X. W. Ma, "Automated crack assessment and quantitative growth monitoring," *Comput.-Aided Civil Infrastruct. Eng.*, vol. 36, no. 5, pp. 656–674, 2021, doi: 10.1111/mice.12626.

[12] Y. Zhang and K. Yuen, "Crack detection using fusion features-based broad learning system and image processing," *Comput.-Aided Civil Infrastruct. Eng.*, vol. 36, no. 12, pp. 1568–1584, Dec. 2021, doi: 10.1111/mice.12753.

[13] S. Dorafshan, R. J. Thomas, and M. Maguire, "Comparison of deep convolutional neural networks and edge detectors for image-based crack detection in concrete," *Construct. Building Mater.*, vol. 186, pp. 1031–1045, Oct. 2018, doi: 10.1016/j.conbuildmat.2018.08.011.

[14] M. R. Jahanshahi and S. F. Masri, "A new methodology for non-contact accurate crack width measurement through photogrammetry for automated structural safety evaluation," *Smart Mater. Struct.*, vol. 22, no. 3, 2013, Art. no. 035019, doi: 10.1088/0964-1726/22/3/035019.

[15] J. Zhang, G. Y. Tian, A. M. J. Marindra, A. I. Sunny, and A. B. Zhao, "A review of passive RFID tag antenna-based sensors and systems for structural health monitoring applications," *Sensors*, vol. 17, no. 2, p. 265, 2017, doi: 10.3390/s17020265.

[16] D. He, Y. Cui, F. Ming, and W. Wu, "Advancements in passive wireless sensors, materials, devices, and applications," *Sensors*, vol. 23, no. 19, p. 8200, 2023, doi: 10.3390/s23198200.

[17] S. R. Patre, "Passive chipless RFID sensors: Concept to applications—A review," *IEEE J. Radio Freq. Identificat.*, vol. 6, pp. 64–76, 2022, doi: 10.1109/JRFID.2021.3114104.

[18] N. Khalid, R. Mirzavand, H. Saghlatoon, M. M. Honari, and P. Mousavi, "Three-port zero-power RFID flood sensor for IoT applications," in *Proc. IEEE Wireless Power Transfer Conf. (WPTC)*, 2020, pp. 61–64.

[19] F. Nekoogar and F. Dowla, "Passive RFID for IoT using UWB/UHF hybrid signaling," in *Proc. IEEE/ACES Int. Conf. Wireless Inf. Technol. Syst. (ICWITS), Appl. Comput. Electromagn. (ACES)*, 2016.

[20] A. Khanna and S. Kaur, "Internet of Things (IoT), applications and challenges: A comprehensive review," *Wireless Pers. Commun.*, vol. 114, no. 2, pp. 1687–1762, Sep. 2020, doi: 10.1007/s11277-020-07446-4.

[21] X. Li, S. Xue, L. Xie, and G. Wan, "A miniaturized passive wireless patch antenna sensor for structural crack sensing," *Struct. Health Monit.*, early access, 2024, Art. no. 215187989, doi: 10.1177/14759217241227797.

[22] X. Li, S. Xue, L. Xie, and G. Wan, "Simultaneous crack and temperature sensing with passive patch antenna," *Struct. Health Monit.*, early access, 2023, doi: 10.1177/14759217231184115.

[23] S. T. Xue, Z. R. Yi, L. Y. Xie, G. C. Wan, and T. Ding, "A passive wireless crack sensor based on patch antenna with overlapping sub-patch," *Sensors*, vol. 19, no. 19, p. 4327, 2019, doi: 10.3390/s19194327.

[24] R. Bhattacharyya, C. Floerkemeier, and S. Sarma, "Towards tag antenna based sensing—An RFID displacement sensor," in *Proc. IEEE Int. Conf. RFID*, Apr. 2009, pp. 95–102, doi: 10.1109/RFID.2009.4911195.

[25] S. Caizzone and E. DiGiampaolo, "Wireless passive RFID crack width sensor for structural health monitoring," *IEEE Sensors J.*, vol. 15, no. 12, pp. 6767–6774, Dec. 2015, 10.1109/JSEN.2015.2457455.

[26] S. Caizzone, E. DiGiampaolo, and G. Marrocco, "Wireless crack monitoring by stationary phase measurements from coupled RFID tags," *IEEE Trans. Antennas Propag.*, vol. 62, no. 12, pp. 6412–6419, Dec. 2014, doi: 10.1109/TAP.2014.2360553.

[27] M. Cui, Z. Wu, Y. Lu, X. Wei, and L. Dai, "Near-field MIMO communications for 6G: Fundamentals, challenges, potentials, and future directions," *IEEE Commun. Mag.*, vol. 61, no. 1, pp. 40–46, Jan. 2023, doi: 10.1109/MCOM.004.2200136.

[28] H. Jiang, B. Xiong, H. Zhang, and E. Basar, "Hybrid far- and near-field modeling for reconfigurable intelligent surface assisted V2V channels: A sub-array partition based approach," *IEEE Trans. Wireless Commun.*, vol. 22, no. 1, pp. 8290–8303, Nov. 2023, doi: 10.1109/TWC.2023.3262063.

[29] L. Xie, T. Wu, Z. Yi, X. Fu, W. Zang, and W. Lu, "Passive accelerometer using unstressed patch antenna interrogated by FMCW radar," *IEEE Sensors J.*, vol. 23, no. 15, pp. 16672–16682, Aug. 2023, doi: 10.1109/JSEN.2023.3284401.

[30] K. Sawa and M. Hasegawa, "Recent researches and new trends of electrical contacts," *IEICE Trans. Electron.*, vol. E83C, no. 9, pp. 1363–1376, 2000.

[31] R. Sharma, A. Jaiswal, V. K. Jha, A. V. Ullas, G. Ji, and R. Prakash, "Drop cast coating of leather dye on copper and investigation of its corrosion behavior in sodium chloride solutions," *Mater. Today, Proc.*, vol. 62, pp. 2965–2969, 2022.

[32] C. Teng, Y. Lin, Y. Tan, J. Liu, and L. Wang, "Facile assembly of a large-area BNNSs film for oxidation/corrosion-resistant coatings," *Adv. Mater. Interfaces*, vol. 5, no. 19, 2018, Art. no. 1800750, doi: 10.1002/admi.201800750.

[33] R. S. Timsit, "High speed electronic connectors: A review of electrical contact properties," *IEICE Trans. Electron.*, vol. E88C, no. 8, pp. 1532–1545, 2005, doi: 10.1093/ietele/e88-c.8.1532.

[34] M. Andrusca, M. Adam, R. Burlica, A. Munteanu, and A. Dragomir, "Considerations regarding the influence of contact resistance on the contacts of low voltage electrical equipment," in *Proc. 2016 Int. Conf. Expo. Elect. Power Eng. (EPE)*, 2016.

[35] X. I. A. Yanqiu, H. A. N. Yu, and F. Xin, "The research progress on lubrication and electrical conductivity of ionic liquids," *Tribology*, vol. 36, no. 6, pp. 794–802, 2016.

[36] H. Liu, H. Ji, H. Hong, and H. Younes, "Tribological properties of carbon nanotube grease," *Ind. Lubrication Tribol.*, vol. 66, no. 5, pp. 579–583, 2014, doi: 10.1108/ILT-08-2012-0071.

Liyu Xie (Member, IEEE) received the B.S. and M.S. degrees in mechanics engineering from Tongji University, Shanghai, China, in 2000 and 2003, respectively, and the Ph.D. degree in system design engineering from Keio University, Tokyo, Japan, in 2009.

Since 2009, he has been with the College of Civil Engineering, Tongji University, where he is currently an Associate Professor. His current research focuses on smart sensors, structural health monitoring, and structural vibration control.

Zeyu Li received the B.S. degree in civil engineering from Central South University, Changsha, Hunan, China, in 2022. He is currently pursuing the master's degree in civil engineering with Tongji University, Shanghai, China.

His current research interests include smart sensors for the structural health monitoring and sensor performance.

Songtao Xue received the B.S. degree in mechanics engineering from Tongji University, Shanghai, China, in 1985, and the M.S. and Ph.D. degrees in structural engineering from Tohoku University, Sendai, Japan, in 1989 and 1991, respectively.

In 1991, he was an Assistant Professor with the Department of Architecture, Tohoku University, and then was promoted to an Associate Professor in 1995. Since 1996, he has been with Tongji University, where he is a Full Professor until now. In 2010, he joined the Department of Architecture, Tohoku Institute of Technology, Sendai, where he is currently the Director. His research focuses on structural health monitoring, seismic engineering, and structural vibration control.

Wensheng Lu received the B.S. degree from Zhejiang University, Hangzhou, China, in 1988, and the M.S. and Ph.D. degrees from Tongji University, Shanghai, China, in 1991 and 2011, respectively, all in civil engineering.

Since 1991, he has been with the College of Civil Engineering, Tongji University, where he is currently a Professor. His current research focuses on seismic testing method of structural and nonstructural components and the safety issues related to building moving technologies.

Guochun Wan (Member, IEEE) received the M.S. and Ph.D. degrees in transportation information engineering and control from Tongji University, Shanghai, China, in 2005 and 2011, respectively.

He became an Associate Professor with Tongji University in 2002. He joined the Department of Electronic Science and Technology, Tongji University, in 2006. His current research interests include signal and information processing, with an emphasis on error-correcting coding, very large scale integrated circuits (VLSI) architectures, radio frequency identification (RFID) strain sensor, and system-on-chip design for communications and coding theory applications.

Wei Zang received the B.E. degree in applied electronic technology from Shanghai Second Industrial University, Shanghai, China, in 1991.

In 2003, he began working with the State Key Laboratory of Modern Technology for Urban Planning and Design, Tongji University, Shanghai, China. Since 2010, he has been the Deputy Director of the Office of the Key Laboratory of Ecology and Energy Saving Study of Dense Habitat, Ministry of Education, Shanghai. His current research interests focus on building technology.